AFRL-ML-WP-TP-2006-464

HIGH-RESOLUTION OF ELECTRON MICROSCOPY OF MONTMORILLONITE AND MONTMORILLONITE/EPOXY NANOCOMPOSITES

Lawrence F. Drummy, Karen Farmer, Ashley Tan, B.L. Farmer, and Richard A. Vaia (AFRL/MLBP)
Hilmar Koerner (University of Dayton Research Inst.)

SEPTEMBER 2005

Approved for public release; distribution is unlimited.

STINFO COPY

**MATERIALS AND MANUFACTURING DIRECTORATE
AIR FORCE RESEARCH LABORATORY
AIR FORCE MATERIEL COMMAND
WRIGHT-PATTERSON AIR FORCE BASE, OH 45433-7750**

REPORT DOCUMENTATION PAGE

1. REPORT DATE *(DD-MM-YY)*	2. REPORT TYPE	3. DATES COVERED *(From - To)*
September 2005	Journal Article Postprint	

4. TITLE AND SUBTITLE

HIGH-RESOLUTION OF ELECTRON MICROSCOPY OF MONTMORILLONITE AND MONTMORILLONITE/EPOXY NANOCOMPOSITES

5a. CONTRACT NUMBER
In-House

5b. GRANT NUMBER

5c. PROGRAM ELEMENT NUMBER
62102F

6. AUTHOR(S)

Lawrence F. Drummy, Karen Farmer, Ashley Tan, B.L. Farmer, and Richard A. Vaia (AFRL/MLBP)
Hilmar Koerner (University of Dayton Research Inst.)

5d. PROJECT NUMBER
4347

5e. TASK NUMBER
RG

5f. WORK UNIT NUMBER
M01R1000

7. PERFORMING ORGANIZATION NAME(S) AND ADDRESS(ES)

Polymer Branch (AFRL/MLBP)
Nonmetallic Materials Division
Materials and Manufacturing Directorate
Air Force Research Laboratory, Air Force Materiel Command
Wright-Patterson AFB, OH 45433-7750

University of Dayton Research Inst.
300 College Park, Dayton OH 45469

8. PERFORMING ORGANIZATION REPORT NUMBER

AFRL-ML-WP-TP-2006-464

9. SPONSORING/MONITORING AGENCY NAME(S) AND ADDRESS(ES)

Materials and Manufacturing Directorate
Air Force Research Laboratory
Air Force Materiel Command
Wright-Patterson AFB, OH 45433-7750

10. SPONSORING/MONITORING AGENCY ACRONYM(S)
AFRL-ML-WP

11. SPONSORING/MONITORING AGENCY REPORT NUMBER(S)
AFRL-ML-WP-TP-2006-464

12. DISTRIBUTION/AVAILABILITY STATEMENT
Approved for public release; distribution is unlimited.

14. ABSTRACT

Using high resolution transmission electron microscopy the structure and morphology of montmorillonite (MMT), a material of current interest for use in polymer nanocomposites, was characterized. Using both imaging theory and experiment, the procedures needed to generate lattice images from MMT were established. These procedures involve careful control of the microscope's objective lens defocus to maximize contrast from features of certain size, as well as limiting the total dose of electrons received by the sample. Direct images of the MMT lattice were obtained from the neat Na^+ MMT, organically modified MMT, and organically modified MMT/epoxy nanocomposites. The degree of crystallinity and turbostratic disorder were characterized using electron diffraction and high resolution electron microscopy (HREM). Also, the extent of the MMT sheets to bend when processed into an epoxy matrix was directly visualized. A minimum radius of curvature tolerable for a single MMT sheet during bending deformation was estimated to be 15 nm, and from this value a failure strain was calculated. HREM can be used to improve the understanding of the structure of polymer nanocomposites at the nanometer length scale.

15. SUBJECT TERMS
Montmorillonite (MMT), nanocomposites, polymers

16. SECURITY CLASSIFICATION OF:			17. LIMITATION OF ABSTRACT:	18. NUMBER OF PAGES	19a. NAME OF RESPONSIBLE PERSON (Monitor)
a. REPORT	**b. ABSTRACT**	**c. THIS PAGE**	SAR	18	Richard Vaia
Unclassified	Unclassified	Unclassified			19b. TELEPHONE NUMBER *(Include Area Code)* (937) 255-9184

High-Resolution Electron Microscopy of Montmorillonite and Montmorillonite/Epoxy Nanocomposites

Lawrence F. Drummy, Hilmar Koerner,[†] Karen Farmer, Ashley Tan, B. L. Farmer, and Richard A. Vaia*

Air Force Research Laboratory, Materials and Manufacturing Directorate,
Wright Patterson Air Force Base, Ohio 45433

Received: June 10, 2005; In Final Form: July 19, 2005

With the use of high-resolution transmission electron microscopy the structure and morphology of montmorillonite (MMT), a material of current interest for use in polymer nanocomposites, was characterized. Using both imaging theory and experiment, the procedures needed to generate lattice images from MMT were established. These procedures involve careful control of the microscope's objective lens defocus to maximize contrast from features of a certain size, as well as limiting the total dose of electrons received by the sample. Direct images of the MMT lattice were obtained from neat Na^+ MMT, organically modified MMT, and organically modified MMT/epoxy nanocomposites. The degree of crystallinity and turbostratic disorder were characterized using electron diffraction and high-resolution electron microscopy (HREM). Also, the extent of the MMT sheets to bend when processed into an epoxy matrix was directly visualized. A minimum radius of curvature tolerable for a single MMT sheet during bending deformation was estimated to be 15 nm, and from this value a critical failure strain of 0.033 was calculated. HREM can be used to improve the understanding of the structure of polymer nanocomposites at the nanometer-length scale.

Introduction

Organic/inorganic nanocomposites have shown extraordinary promise as high-performance materials over the past decade. Layered silicate materials, such as montmorillonite (MMT), have attracted significant interest as inorganic filler materials because of their ability to be separated into single 1 nm thick platelets. When they are properly processed into a polymer matrix, significant improvements in several properties are seen with relatively low additions of filler material.[1–4] While much early attention toward polymer nanocomposite materials from industry was focused on reinforced thermoplastics,[5,6] thermoset nanocomposites[7–12] have generated recent interest for use in several application areas including aerospace. Processing of MMT into an epoxy matrix is often more challenging than processing it into thermoplastics, mainly because it is difficult to apply sufficient shear forces to the material to uniformly disperse the MMT sheets. Without sufficiently high shear forces (as exist in processing methods such as extrusion or injection molding), dispersion relies on intercalation of epoxy monomer between the MMT layers and swelling of the interlayer spacing during curing of the matrix. This leads to morphologies consisting of highly swollen MMT tactoids that retain their overall registry and are reminiscent of the unintercalated stacks. Various mechanical properties (modulus, strength, and toughness) depend on morphology on different length scales. It is therefore necessary to develop sophisticated morphology characterization techniques in order to improve the quantitative description of structure on these length scales and enable establishment of the processing/structure/properties relationship.

Montmorillonite has been the focus of numerous research reports on polymer nanocomposite materials, and it has many characteristics that are beneficial for use in this application. These characteristics include a high inherent stiffness (bulk modulus $\sim$ 270 GPa [13]) and the ability to be dispersed in and bond to a polymer matrix using surface modification techniques. The detailed ultrastructural characterization of polymer/layered silicate nanocomposite materials requires a combination of experimental techniques, including X-ray scattering and transmission electron microscopy. Because the properties of these materials depend on both the degree of intercalation of the polymer between individual clay sheets and the interfacial interactions between the polymer and those clay sheets, characterization must be performed that is sensitive to structure on the nanometer-length scale. While X-ray diffraction (XRD) and other global techniques can give information on the nanometer-length scale, they measure over large sample areas, and therefore local structural details are averaged out. To characterize the local degree of MMT dispersion, the quality of interface, and the MMT inherent internal perfection, high-resolution electron microscopy (HREM) must be used. Because these materials are bulk structural materials, however, real-space characterization (microscopy) of nanocomposites must be performed over large enough areas of sample to ensure that an accurate picture of the global microstructure is obtained.

HREM has provided new insights into the microstructure of a wide array of technologically relevant materials, including inorganic,[14–16] organic,[17–20] and nanocomposite, or "hybrid", materials, such as bone.[21,22] Interesting examples of the application of HREM to the study of nanoparticles include the observation of defects in carbon nanotubes,[23–25] as well as determination of the symmetry of CdSe quantum dots.[26] Researchers have used HREM for the characterization of layered silicates and other clay minerals,[14] and transmission electron microscopy (TEM) for polymer/layered silicate nanocomposites.[27–29] While the results obtained have been useful for each particular study, the experimental techniques necessary

---

* Corresponding author. E-mail: richard.vaia@wpafb.af.mil.
† Present address: University of Dayton Research Institute, Dayton, OH 45469.

to generate and interpret HREM lattice images from MMT in nanocomposites have not been established. HREM imaging of polymer/layered silicate nanocomposites presents some challenges that are somewhat similar to the challenges of HREM imaging of polymer crystals, and these will be discussed in detail. In particular, they involve the direct imaging of large lattice plane spacings (>1 nm) and small lattice plane spacings (<0.5 nm) at the same time, and HREM imaging of crystalline materials that are sensitive to electron beam exposure. Here we report the direct imaging of the montmorillonite (MMT) lattice in neat Na$^+$ MMT samples, organically modified MMT (OMMT), and OMMT dispersed in an epoxy matrix. The experimental conditions used to generate these images will be described in detail. HREM imaging of MMT sheets in several orientations allows for a more detailed, three-dimensional understanding of the local structure of nanocomposite materials to be developed.

Experimental Section

Nanocomposites, MMT suspensions, and organically modified montmorillonite (OMMT) suspensions were prepared using Cloisite Na$^+$, Cloisite 6A, Cloisite 20A (OMMT, cation exchange capacity = 92 mequiv/100 g, dimethyl ditallow ammonium bromide, Southern Clay Products, Inc.), and Nanocor I30E (cation exchange capacity = 145 mequiv/100 g montmorillonite, octadecylammonium bromide, Nanocor). The thermoset matrix consisted of Epon 862 (bisphenol F epoxy) with aromatic diamine (Epikure W, Resolution Performance Products) at a 100:26 ratio.

The nanocomposite fabrication procedure followed that reported by Koerner et al.[11] In brief, OMMT was dispersed in the epoxy monomer with a high shear mixer. After additional short mixing with curing agent W and subsequent degassing, a two-stage curing reaction (120 °C for 2 h; 175 °C for 2 h) was used. Differential scanning calorimetry (TA Instruments Q1000) verified complete cure for all concentrations of OMMT.

For transmission electron microscopic (TEM) analysis, dilute (<0.001%) suspensions of Na$^+$ MMT in water and 20A OMMT in toluene were cast onto amorphous carbon support films that were approximately 10−20 nm in thickness. For TEM analysis of nanocomposites, ultrathin sections of the silicate/epoxy samples were cut using a RMC PowerTome XL ultramicrotome equipped with a Diatome diamond knife. A cutting speed of 1 mm/s was used to cut 50 nm thick sections at room temperature. Sections were collected on 400 mesh copper grids. The sections were then coated with a thin layer (~10 nm) of amorphous carbon to improve the stability of the sections during electron irradiation.

HREM images were generated on a Phillips CM200 FEG operating at 200 kV. Images were recorded on Kodak SO-163 film and a 1024 × 1024 cooled Gatan CCD at magnifications of 80K−225K×. Negatives were digitized using a Minolta DiMAGE scanner at resolutions of 2400 and 4800 dpi. Image gray scales were adjusted for optimum contrast; however, images were not rescaled in size or rotated as these operations can induce artifacts. Fast Fourier transformations (FFTs) were calculated from image regions of size 512 × 512 pixels up to 4096 × 4096 pixels using the Scion Image software. Fourier filtering was done by placing a finite sized mask over only the crystalline reflections in the FFTs, and performing an inverse FFT using only the intensity inside the masked regions.[30] A Delong Instruments LVEM5 operating at accelerating voltages near 5 kV was used to collect low-voltage electron micrographs.

Calculations of the effects of microscope operating parameters on the expected image contrast from polymer/MMT nano-

composites were used for comparison with experiment. The microscope parameters used for calculation of the contrast transfer function plots and the multislice image simulations were as follows: electron energy = 200 kV; wavelength = 0.002 508 nm; C_s = 1.2 mm; spread of defocus = 7.5 nm; divergence half-angle = 0.5 mrad. For the calculations, the [100] zone images were simulated using a 6.08 nm × 7.97 nm × 3.61 nm cell size in the a, b, and c directions, respectively (models from ref 38). The thickness in the direction of the propagating beam was therefore 6.08 nm, and this was divided into 20 slices for the multislice calculation. The defocus series simulated was −55 to −500 nm in steps of 17 nm. For the [001] zone simulated defocus series, the same cell and range of defocus was used, and the 3.6 nm thickness in the direction of the beam was divided into 12 slices for the calculation. Mathematica 5.0, the Cerius^2 HREM module, and the EMS online version were used for these calculations.

Results and Discussion

The Results and Discussion are divided into four sections. The first section describes background on phase contrast HREM imaging of extended crystal lattices, and the challenges of applying this technique to polymer/layered silicate nanocomposites. The next section briefly describes the structure of montmorillonite, with references to more detailed work. The third section describes electron beam induced disordering of materials, including MMT. This disordering is discussed in the context of being one limiting factor in the resolution attainable from the HREM imaging of MMT. Finally, the application of HREM to MMT and MMT/epoxy nanocomposites is presented, with emphasis on image interpretation and the direct visualization of local deformation and defect structures.

1. Imaging Theory: HREM Imaging of Extended Crystal Lattices. For samples that are sufficiently thin, the contrast in HREM images is linearly related to the projected electronic potential in the sample. Contrast given to crystal lattice planes of a certain d spacing in experimental images is governed by the contrast transfer function (CTF) of the microscope. The CTF describes an operation performed on the electrons that exit the sample by the objective lens of the microscope. An ideal CTF would remain constant for all values of the reciprocal space vector magnitude k, and would decay rapidly to zero at a value of k defining the ultimate resolution of the microscope. In practice the transfer function has peaks and zeros and eventually decays to zero at a value of k much less than the reciprocal of the electron wavelength. When the CTF is negative, positive phase contrast results and regions of high electron density appear dark against a bright background. When the CTF is positive, negative phase contrast results and electron dense regions appear bright against a dark background. The experimental two-dimensional CTF can be visualized by HREM images of amorphous thin films. The background of the FFT (excluding the crystalline reflections) consists of diffuse concentric rings, and the intensity profiles of these rings are directly related to the square of the CTF. The exact form of this function at a particular value of defocus depends on the electron wavelength and the spherical aberration coefficient of the objective lens.

The CTF is well approximated by the function $\sin[\chi(k,\Delta f)]$, where $\chi(k,\Delta f)$ is defined as

$$\chi(k,\Delta f) = \pi \Delta f \lambda k^2 + \frac{1}{2}\pi C_s \lambda^3 k^4$$

k is the reciprocal space vector magnitude, Δf is the defocus, C_s is the spherical aberration coefficient of the microscope's
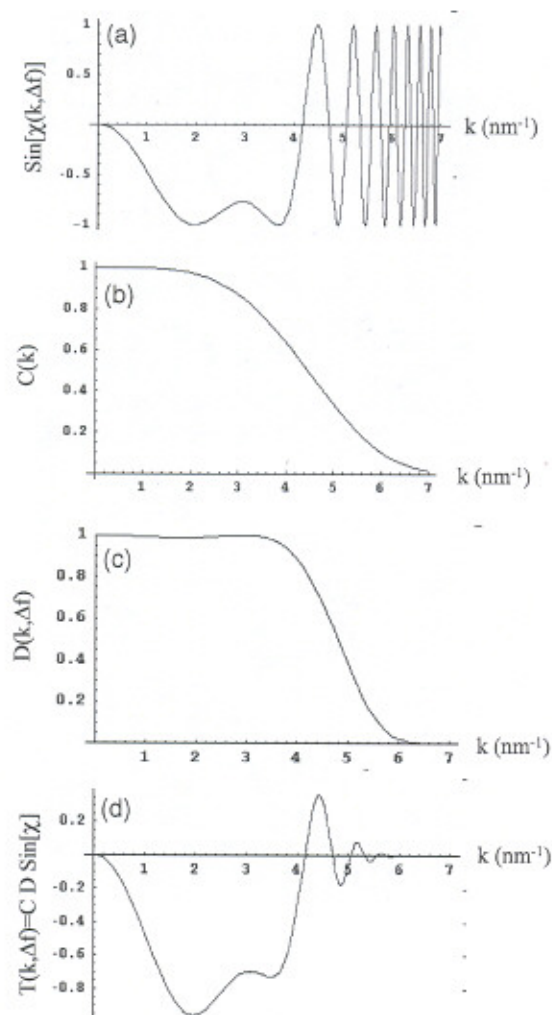
Figure 1. (a) Plot of $\sin[\chi(k,\Delta f)]$ at Scherzer defocus (-65 nm) for a microscope operating at 200 kV. (b) Plot of $C(k)$, the chromatic aberration envelope function, which is independent of defocus. (c) $D(k,\Delta f)$, the divergence envelope function at Scherzer defocus. (d) $T(k,\Delta f)$, the total transfer function, is the product of the curves shown in parts a, b, and c.

objective lens, and λ is the wavelength of the incident electrons.[31-33] The microscope performs best, that is the CTF approaches an ideal form, at Scherzer defocus. The value of Scherzer defocus, where the first zero is as far out in k-space as possible, is given by[32]

$$\Delta f_{\text{Scherzer}} = -1.2(C_s\lambda)^{1/2}$$

Figure 1 shows a plot of $\sin[\chi]$ for the Philips CM200 at Scherzer defocus. A significant amount of contrast is measurable out to $k = 4$ nm^{-1}, or $d = 0.25$ nm. However, for low values of k, or large d spacings, the contrast is very low at Scherzer defocus.

The total transfer function, $T(k,\Delta f)$, also includes the chromatic and divergence envelope functions. The chromatic aberration envelope function, $C(k)$, is dependent on the microscope's spread of defocus, δ, but not on the magnitude of the defocus itself.

$$C(k) = \exp\left(-\frac{1}{2}\pi^2\lambda^2\delta^2 k^4\right)$$
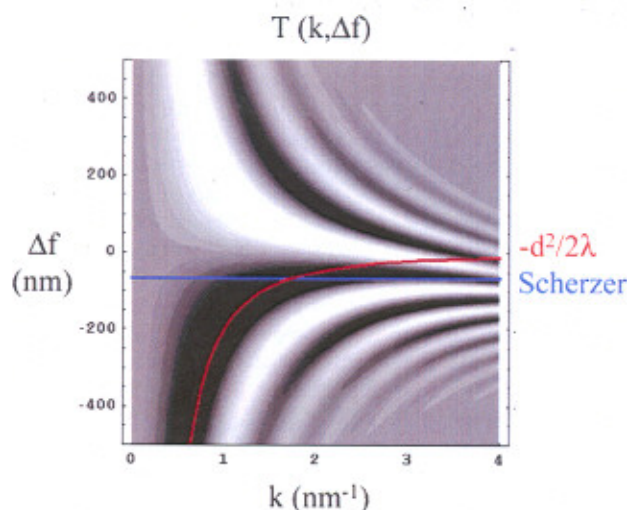
Figure 2. Density plot of $T(k,\Delta f)$. Here black regions correspond to values of positive phase contrast, white regions correspond to negative phase contrast, and gray regions correspond to near zero contrast. Scherzer focus ($\Delta f = -65$ nm) and the position of the first zero in T ($-d^2/2\lambda$) are overlaid.

The divergence envelope function, $D(k,\Delta f)$ is dependent on both the beam divergence half-angle, α, and the defocus, Δf.

$$D(k,\Delta f) = \exp(-\pi^2\alpha^2(\Delta f|k| + C_s\lambda^2|k|^3)^2)$$

The total transfer function of the microscope is then equal to the product of the chromatic aberration envelope function, the divergence envelope function, and the function $\sin[\chi]$:

$$T(k,\Delta f) = C(k)\, D(k,\Delta f)\, \sin[\chi(k,\Delta f)] \qquad \text{(refs 31-33)}$$

The microscope's total transfer function, $T(k,\Delta f)$, is also plotted in Figure 1 at a defocus value of -65 nm. With the envelope functions included, it can be seen that detectable contrast for subnanometer d spacings, such as lattice spacings within a layered silicate sheet, can be obtained only near zero focus, and to obtain positive phase contrast the microscope must be at Scherzer focus.

Polymer/layered silicate nanocomposites, though, can have much larger d spacings ($\gg 1$ nm), and these are the intersheet spacings. To obtain good contrast at large d spacings, a defocus value of $-d^2/2\lambda$ must be used. It closely follows the first minimum in the CTF for small values of k. As the lattice plane spacing of interest increases to 3 nm, the defocus necessary to maximize contrast between the layers is 1800 nm for a microscope operating at 200 kV. If the lattice plane spacing is 10 nm, the optimum defocus is 20 000 nm. d spacings of 10 nm or larger are routinely measured using small-angle X-ray scattering and Fourier transform analysis of TEM images from epoxy/layered silicate nanocomposites.[11,12] Defocusing the objective lens to maximize contrast for large d spacings can improve contrast from materials with small changes in thickness or density.[34] However, defocus contrast can introduce some image artifacts that must be accounted for, including the increase of the apparent MMT sheet thickness as well as the appearance of dark and light Fresnel fringes parallel to the sheets that could be misinterpreted as additional sheets.

We can plot $T(k,\Delta f)$ as a density plot at a constant value of λ and C_s to see the expected variations of the microscope contrast as a function of k at different values of defocus (Figure 2). Here black regions correspond to minima in $T(k,\Delta f)$, where strong positive phase contrast results. White regions correspond

to maxima in $T(k,\Delta f)$, where strong negative phase contrast results. Gray regions in the plot have values of $T(k,\Delta f)$ close to zero, where little contrast is obtained. Two different focus settings, both of which are useful for HREM imaging of polymer/layered silicate nanocomposites, are overlaid. Scherzer defocus, for a 200 kV microscope with $C_s = 1.2$ mm, is -65 nm. At Scherzer defocus and for small values of k, $T(k,\Delta f)$ goes to zero (little contrast is obtained). Also overlaid with the density plot is the $-d^2/2\lambda$ focus condition, which closely follows the first minimum in $T(k,\Delta f)$ for small values of k. The crossover defocus, where the $-d^2/2\lambda$ focus condition is equal to the Scherzer defocus condition, is approximately 0.6 nm. For k values smaller than the crossover value, high contrast is obtained using $-d^2/2\lambda$. It can readily be seen that for k values larger than the crossover value, however, the contrast in the image deviates from ideal at the $-d^2/2\lambda$ focus setting, and Scherzer defocus must be used. The existence of these two conflicting focus settings implies that the simultaneous HREM imaging of both the inter- and intrasheet lattice spacings in polymer/layered silicate nanocomposites will present challenges; however, with careful understanding and application of proper focusing techniques a great deal of information can be extracted from experimental images.

The prior discussion primarily focuses on the manipulation of the transfer function $T(k,\Delta f)$ of the objective lens to maximize contrast from features of a certain size. Other methods to maximize contrast are also useful. For example, contrast may be increased with the use of an objective aperture to block out diffracted beams scattered at high angles. Lowering the accelerating voltage can dramatically increase contrast; however, resolution will be lowered.[35,36] Zero-loss filtering can also be used to improve the contrast obtained from polymeric materials.[37] For all of these techniques, however, contrast in the image is still determined by the transfer function. For HREM imaging of polymer/layered silicate nanocomposites, the microscope must have a high accelerating voltage, be well-aligned, and be focused at the Scherzer defocus condition with no objective aperture (or an aperture of sufficient size so that all of the diffracted beams of interest are used to form the image).

2. Structure of Montmorillonite. Montmorillonite (MMT) is a member of the smectite family of clay minerals consisting of 1 nm thick, hydrophilic aluminosilicate layers that are approximately 100−200 nm in lateral extent. The general chemical formula for layered aluminosilicates such as mica, MMT, and pyrophylite is $[Si_4O_8][Al_2O_2(OH)_2]$, with an octahedrally coordinated aluminohydroxide layer bound by two tetrahedrally coordinated silica layers. In MMT the aluminosilicate sheets have charge defects in the octahedral layer, balanced by positive cations in the van der Waals gallery between the layers. MMT predominantly has Al → Mg defects in the octahedral layer, modifying their chemical structure to give approximately $Na_{0.4}[Si_4O_8][Al_{1.6}Mg_{0.4}O_2(OH)_2]$.[38] The Na^+ ions on the surface of the aluminosilicate layers can be exchanged with organic surfactants to decrease hydrophilicity. Figure 3 shows a molecular model of the structure in two orientations.

The MMT crystal structure is monoclinic ($C2/m$) with lattice parameters $a = 0.52$ nm, $b = 0.89$ nm, $c = 0.95-1.00$ nm, and $\beta = 95-100°$.[39] Although a three-dimensional unit cell and space group are often quoted for this material, it is generally well understood that the structure lacks long-range, three-dimensional translational order. In reality the structure is turbostratic, with little or no correlations between stacked layers.[40] This is supported by X-ray diffraction, which shows
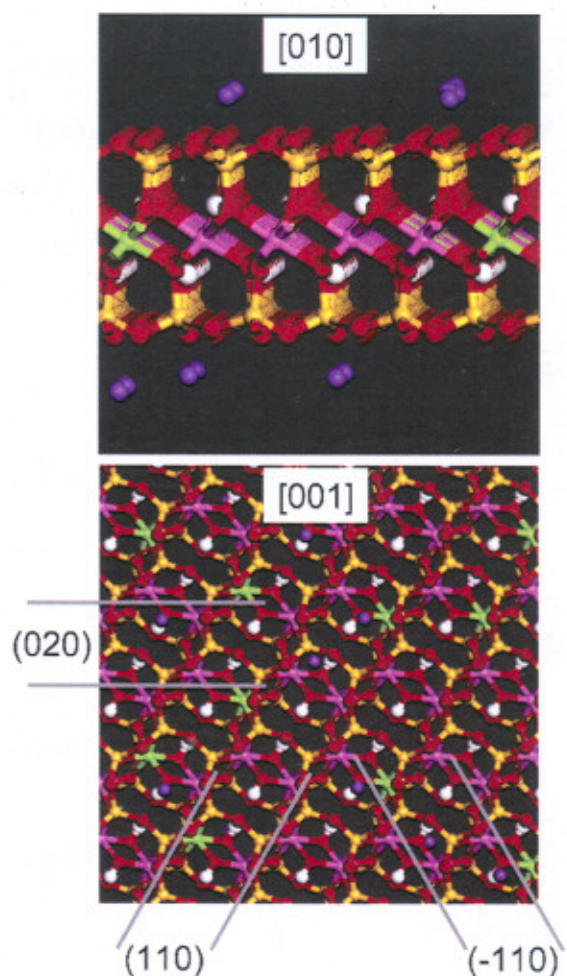
Figure 3. [010] and [001] projections of the montmorillonite lattice. Atom color codes: Si, orange; Al, light purple; O, red; H, white; Mg, green; Na, dark purple.
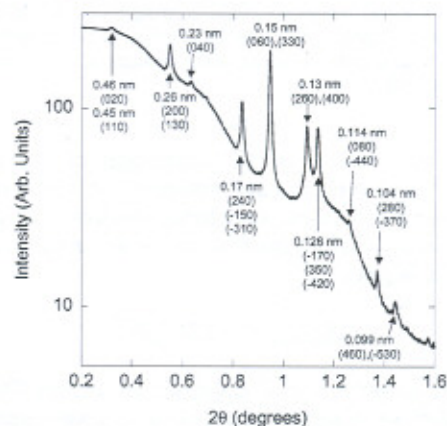
Figure 4. Intensity profile of an electron diffraction pattern taken from 6A OMMT. Several peaks are identified, all of which can be indexed as ($hk0$)-type reflections from the MMT lattice. The 200 kV electrons have a wavelength of 0.0025 nm.

no evidence for (hkl)-type reflections in powder patterns.[41,42] Figure 4 shows one quadrant of an electron diffraction pattern taken from Cloisite 6A OMMT with the direction of the beam normal to the OMMT sheets. Similar patterns are obtained from Cloisite Na^+ and 20A. Every reflection can be indexed as ($hk0$) type,[43] and electron and X-ray diffraction patterns taken from

samples with powder orientation show only (00*l*) reflections and these (*hk*0) type reflections.

3. Electron Beam Sensitivity of Montmorillonite. HREM imaging and electron diffraction (ED) of beam-sensitive materials has been reviewed by several researchers.[17-20,44] When characterizing a new material by HREM or ED, it is desirable to calculate the critical dose of electrons needed for destruction of crystallinity in the sample, commonly given in units of coulombs (C) per square centimeter. It is then necessary to keep the total dose received at the sample during imaging well below this critical dose. Techniques can be used that limit the dose of electrons so that the sample is irradiated only during imaging.[18] The ultimate resolution attainable from a beam-sensitive material is often limited by its critical dose, not the optics of the microscope.

Kumar and Adams[45] found a correlation between the electron beam stability of various crystalline polymers and their thermal melting or degradation temperature. Figure 4 shows an electron diffraction pattern from Cloisite 6A OMMT cast from toluene onto an amorphous carbon support film. We have found the degree of crystallinity in MMT to be sensitive to electron beam exposure, with the outer wide-angle reflections ($d < 0.15$ nm) in the ED pattern beginning to fade at a dose of approximately 20 C/cm^2, and the inner wide-angle reflections ($d = 0.45$ nm; (110), (200) reflections) fading at approximately 100 C/cm^2. The crystalline reflections appear to fade uniformly over this range of electron dose, from the outside of the pattern in. The dose of electrons (D) received at the sample can be calculated with knowledge of the microscope operating parameters according to the relationship

$$D = jtM^2$$

where j is the screen current density, t is the exposure time, and M is the magnification.[18] This means that, at typical HREM imaging conditions for inorganic materials ($M = 300\,000$, $j = 100$ pA/cm^2), measurable beam damage would occur in approximately 2 s, and the critical dose (100 C/cm^2) would be reached within 10 s of irradiation. Using typical low-dose imaging conditions ($M = 80\,000$, $j = 10$ pA/cm^2), damage would not begin to occur for 5 min, and the critical dose would not be reached for 25 min. Gu et al.[46] have measured the critical dose in K$^+$ MMT, nontrite, and saponite to be 21, 99, and 27 C/cm^2, respectively. The difference in MMT beam stability measured by Gu and co-workers and in this work may be due to slight differences in chemical structure (K$^+$ instead of Na$^+$ cations), cation exchange capacity, defect content, or processing history of the material. The critical dose also depends on the incident electron energy[36] and in some cases the dose rate, although these values were similar in both cases and therefore are not expected to be the cause of the difference.

According to Grim,[43] who examined the thermal behavior of many types of smectites including montmorillonite, there are several stages of physical and chemical changes that take place in the MMT lattice during heating. The first is loss of adsorbed water between the MMT layers, occurring at temperatures of 100−200 °C. With further temperature increase, dehydroxylation occurs from the internal lattice of the aluminosilicate layer at approximately 500−800 °C. According to X-ray diffraction analysis the MMT remains crystalline throughout this process, with only slight rearrangements detected.[47,48] After these two changes, both corresponding to endotherms in differential thermal calorimetry, a third endotherm often occurs in montmorillonites at temperatures of 800−900 °C that can be correlated with the destruction of the lattice. The critical dose
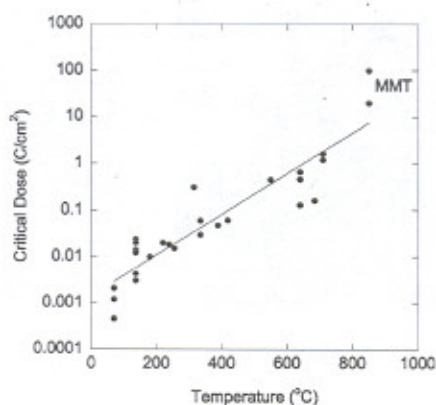
Figure 5. Critical dose of electrons for destruction of crystallinity in polymers[45] and montmorillonite, correlated with their melting temperatures.

of MMT (100 C/cm^2) can then be correlated with its thermal melting temperature of ~850 °C. This data point shows a relatively good correlation to the empirical power law previously described for organic materials[45] (shown in Figure 5), with data points for MMT added from this work and the literature.[46]

The correlation in Figure 5 is not intended to suggest a significant temperature rise in the specimen during irradiation, however. Under moderate to low dose irradiation conditions and with thin specimens a significant temperature rise in the sample is not expected.[45,49] Radiation damage mechanisms in solids involve more complex mechanisms than thermal heating. In polymers and organics, particularly those with aromatic structures, damage can be correlated with carbon K-shell ionization events.[36] These events can cause primary bond rupture, forming free radicals leading to chemical cross-linking or other irreversible changes.[50] Polymers with higher thermal stability are in general more electron beam resistant. In semiconductor, ceramic, and oxide structures, damage can also occur, usually at much higher electron doses than in polymers. Amorphization by energetic particles can be explained by the direct impact of a displacement cascade or the accumulation of point defects. The latter mechanism has been suggested to be more important in light ion or electron irradiation.[51,52] A study of radiation damage in Y−Ba−Cu−O high T_c superconductors showed that electron irradiation at incident energies $E < 450$ kV produced significant amounts of oxygen vacancies.[53] It is likely that electron irradiation produces oxygen vacancies in montmorillonite as well, and when a critical concentration of vacancies is reached the structure is rendered amorphous. Naguin and Kelly[54] suggested that amorphization of ceramics should occur for structures with Pauling ionicities ≤0.47, although Wang and Ewing[51,55] have reported the process to occur in materials with ionicities of up to 0.68. The ionicity of a structure is defined as

$$\text{ionicity} = 1 - \exp[-0.25(X_A - X_B)^2]$$

where X_A and X_B are the electronegativities of atoms A and B that form a bond.[56] The average bond ionicity of aluminosilicate materials with a structure [Si$_4$O$_8$][Al$_2$O$_2$(OH)$_2$], such as montmorillonite, is 0.47, and this value places them in the range of materials that should be susceptible to radiation-induced amorphization. Addition of Mg charge defects in place of the Al atoms in moderate amounts (~20%) only raises the average bond ionicity of the structure to 0.48.

4. Application of HREM to Polymer/Layered Silicate Nanocomposite Materials. Sections 1−3 of the paper describe the background and experimental procedures that are necessary
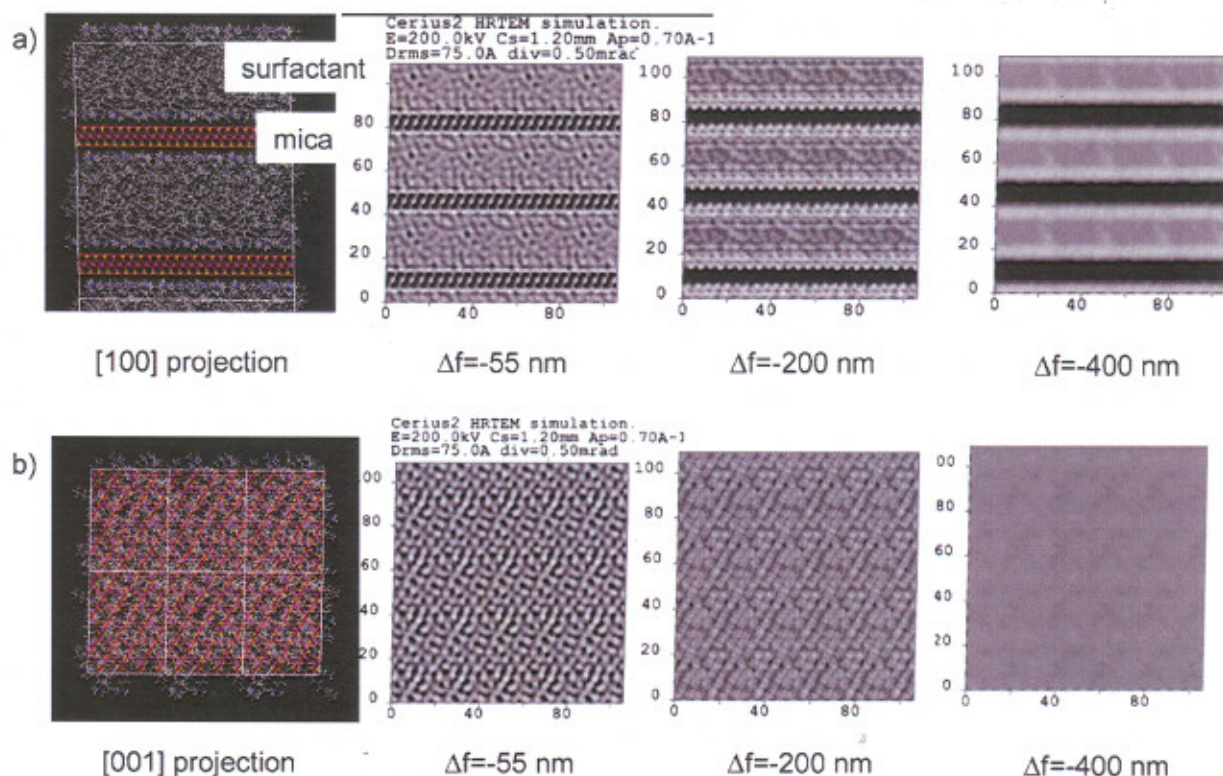
Figure 6. (a) [100] projection of a periodic molecular model of mica/C18 intercalated nanocomposite. Three simulated HREM images at different values of objective lens defocus are shown. The model and the simulated images are shown at slightly different magnifications, so only two MMT layers are visible in the model while three are visible in the simulated images. (b) [001] projection of the model and the corresponding simulated HREM images. $x-y$ axes on the simulated images are in units of angstroms.

when using HREM in the study of polymer/layered silicate nanocomposites. The following demonstrates the application of this technique to various layered silicate and polymer/layered silicate nanocomposite materials. To gain a greater understanding of the effect of microscope operating conditions on the expected image contrast, HREM images of layered silicate/surfactant molecular models were simulated using the multislice method. The multislice method[57-61] of simulating HREM images divides the sample into slices normal to the incident electron beam. The structure is then approximated as a weak phase object, and the contrast in the image is linearly related to the projected electronic potential in the sample by the contrast transfer function. Multiple scattering effects are also accounted for. Figure 6 shows a periodic molecular model of layered silicate sheets (mica shown here) with $C_{18}H_{37}-NH_3^+$ surfactant molecules (C18) between the layers. Mica and MMT have the same general chemical formula (see section 2), and the lattice structure is similar as well, so the results presented in Figure 6 are not expected to be significantly different for mica or for MMT. The number of C18 molecules between the layers is higher than typical OMMTs in this model. The cation exchange capacity of mica is 251 mequiv/100 g, compared to 92 mequiv/100 g for the MMT used in this study. The corresponding values of area per surfactant molecule for mica and MMT are approximately 0.47 and 1.41 nm², respectively. The high exchange capacity results in the surfactant tails having a more extended chain conformation, lying approximately perpendicular to the sheet surface, and this results in a large interlayer spacing (~3 nm). The local density changes in the model are therefore comparable to OMMT intercalated with some polymer material. A defocus series was calculated for two different projections of the model, the [100] direction (parallel to the sheets) and the

[001] direction ($\beta \neq 90°$ in this model, so this direction is close to but not identical to the (001) normal). As the defocus is increased from Scherzer in the [100] projection simulation, the interlayer contrast increases significantly. However, the intrasheet spacings are no longer resolved at −400 nm defocus. Similarly, at −400 nm defocus in the [001] zone axis virtually no contrast is seen, as only the intrasheet lattice spacings are visible in this projection. The results show that focus must be maintained at or near Scherzer focus in order to reproducibly image the small intrasheet spacings. This is often hard to do in practice, however, because at this low value of defocus the contrast between the sheets is extremely low.

Figure 7 shows an experimental defocus series taken at defocus conditions similar to those simulated in Figure 6. There is experimental error in finding Scherzer defocus precisely. The minimum contrast focus setting,[32] which is near zero defocus, can be used to find Scherzer. Live visualization of the CTF using FFTs can also be used to find Scherzer, although this can present difficulties when imaging beam-sensitive materials. At low magnification (Figure 7a,c,e) the contrast in the images clearly improves with increasing defocus. In fact, at Scherzer defocus the sheets themselves are very difficult to see at this magnification. This is why a large defocus is typically used when imaging polymer/layered silicate nanocomposites. The images on the right-hand side (Figure 7b,d,f), which are simply magnified regions of the same images on the left, show that as the defocus is increased from Scherzer the visible fine structure in the image is lost. It should be noted that the total electron dose for all images was kept well below the critical dose. At −200 nm defocus the high-frequency lattice fringes are still resolved, and the contrast from the layers is greatly improved, making this focus setting an apparently good compromise.
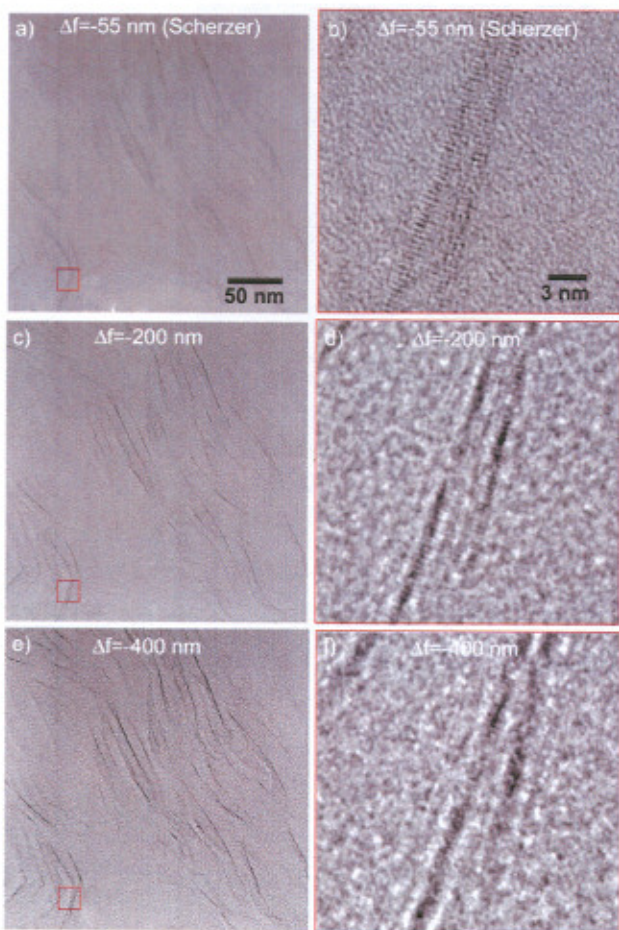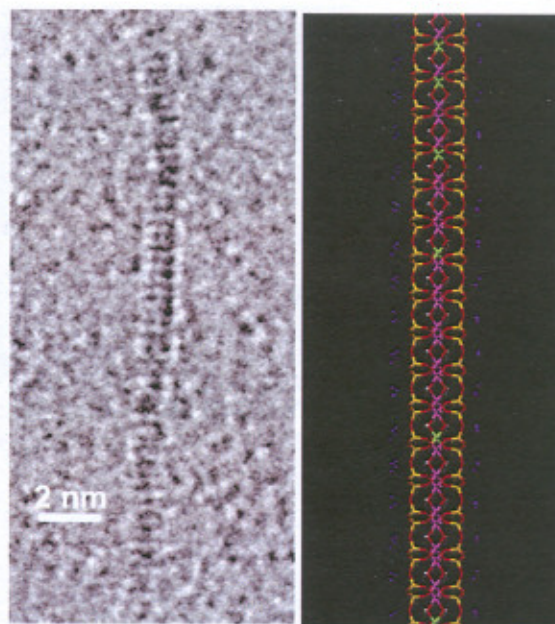
Figure 7. Experimental defocus series of I30E OMMT/epoxy nano-composite at defocus values of approximately −55, −200, and −400 nm. The images on the right-hand side are magnified from the corresponding images on the left.

Figure 8. HREM image of an OMMT sheet embedded in an epoxy matrix, compared with an MMT molecular model.

Figure 9. Low-voltage electron micrograph of 20A OMMT cast from dilute solution onto an electron transparent amorphous carbon film. Regions of individual, 1 nm thick MMT sheets can clearly be seen. An electron diffraction pattern captured from a single sheet on the LVEM is inset.
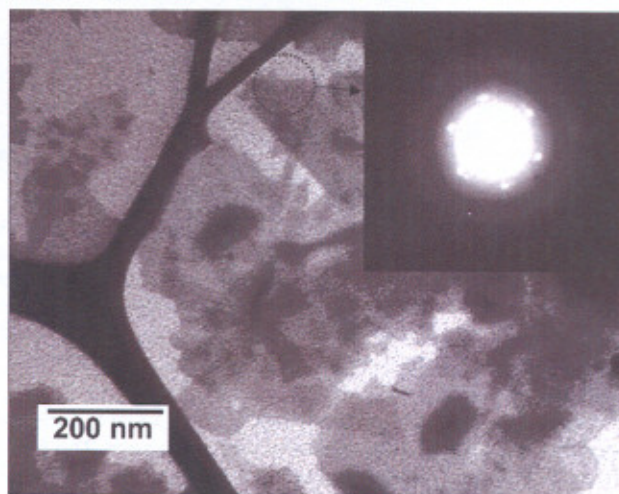
Maintaining reproducible and interpretable contrast from the high-frequency fringes so far from Scherzer defocus is difficult, however. These results demonstrate that it is desirable to focus at Scherzer defocus in order to simultaneously image both the large (intersheet) and small (intrasheet) lattice spacings present in polymer/layered silicate nanocomposites.

Within an exfoliated nanocomposite, single MMT sheets can be imaged in several orientations using the HREM methods described in the previous sections. Figure 8 shows an image of one MMT sheet oriented edge-on in an exfoliated nano-composite. A large amount of intrasheet detail can be seen. The image shows good quantitative agreement with several lattice projections of MMT, as determined from Fourier transform analysis, and it shows the best qualitative agreement with the [350] projection (this projection of the molecular model is shown). With the ability to image intrasheet lattice spacings of MMT sheets in nanocomposites using HREM, sheets in several different orientations can be located and their lateral extent measured. Also, internal lattice defects such as grain boundaries or edge dislocations can be directly visualized using HREM methods. The MMT sheets have a low defect density, most likely due to the high energies associated with such defects, and therefore direct images of these defects are expected to be difficult to obtain. HREM taken from individual sheets demonstrates this low defect density.

We used a solution casting method to prepare MMT and OMMT samples with sheets parallel to the substrate. Low concentrations of Na⁺ MMT and 20A OMMT were dispersed in solvents and cast onto thin amorphous carbon substrates. In the resulting samples, pseudomonolayers of individual, ~1 nm thick, MMT sheets were formed on the electron transparent substrate. Occasional clumps or stacks of the clay sheets were seen; however, it was possible to find large regions of single-layer MMT. The morphology of the resulting films can be generally well understood from the LVEM micrograph shown in Figure 9. The use of low-voltage electron microscopy (LVEM) can considerably increase contrast[36] from the 1 nm thick MMT sheets in plan-view orientation. Micrographs from these samples taken at 200 kV show little contrast. An electron diffraction pattern from a single sheet, obtained on the LVEM from a region of sample approximately the size shown by the dashed circle, is inset in Figure 9. Although this diffraction pattern shows the single-crystalline nature of a single sheet, the

HREM of MMT and MMT/Epoxy Nanocomposites

J. Phys. Chem. B, Vol. 109, No. 38, 2005 **17875**
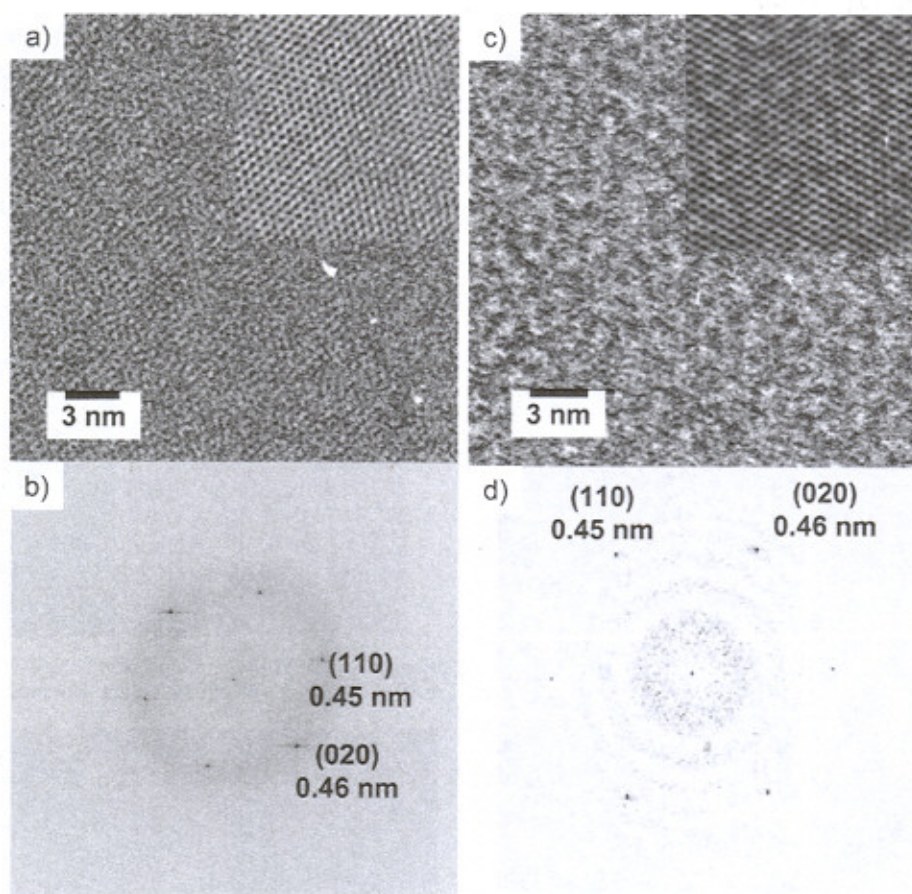
Figure 10. (a) HREM image from a region of single-layer OMMT. The Fourier-filtered image is inset. (b) The power spectrum of the Fast fourier transformation (FFT), taken from the raw HREM image in part a, shows extremely sharp reflections which can be indexed at (110) and (020). (c) HREM image from single-layer Na+ MMT. The Fourier-filtered image is inset. (d) The FFT from part c.

MMT layers exhibit an irregular overall morphology, and faceting of the external sheet edges on low-index lattice planes is rarely observed.

Figure 10a shows a HREM micrograph of 20A OMMT sheets cast from toluene on an amorphous carbon substrate. The FFT from the image, shown in Figure 10b, exhibits the near-hexagonal symmetry of the MMT [001] projection. The Fourier-filtered image is inset in Figure 10a. This was generated by selecting the local area of intensity around the reflections in the FFT, performing an inverse FFT, and overlaying the Fourier-filtered image with the raw image. HREM image simulations were also preformed for the MMT [001] projection (Figure 11), to compare the contrast with experimental images. Good agreement is seen for a defocus of −100 nm. A data set similar to that of Figure 10a,b is shown in Figure 10c,d for Na+ MMT, with no organic surfactant present, cast from water onto an amorphous carbon film. The results are identical, indicating that the lattice fringes do indeed arise from the internal structure of the MMT sheets, and not from any effect of the surfactant. The extremely sharp reflections in the FFTs from these images (Figure 10) show the high degree of order present at the atomic scale within the aluminosilicate sheets themselves. There is no evidence for edge dislocations with Burgers vectors in the plane of the sheets over large regions (several sheets, several hundred nanometers). Occasionally regions are imaged that have low contrast and show only one or two reflections in the FFT, and this is most likely due to slight local changes in orientation of the sample.[18,62]

An HREM image of a stack of OMMT (20A) cast from toluene is shown in Figure 12a. We have seen evidence for uncorrelated, turbostratic-type stacking of OMMT sheets, as can be seen in Figure 12a and the corresponding FFT (below). The image shows no discernible lattice fringes over long ranges, and the FFT shows several peaks at 0.45 nm representing the superposition of several patterns from single sheets, such as the single sheets shown in Figure 10. Figure 12b also shows no long-range lattice fringes, and the FFT also reveals the superposition of several single sheets; however, in this case apparent interlayer correlations are visible. The FFT of Figure 12b clearly shows the stacking of at least six individual OMMT sheets with rotation angles of $n \times (6°)$, where n is an integer. It is possible that the stacking of sheets with $n \times (6°)$ rotational angles is coincidental; however, the regularity in the FFT is striking. The distinction between ordered (where the a and b axes are parallel in successive sheets in a stack), semiordered (orientation defined by $n \times (60°)$ rotations), or turbostatic stacking has been examined in smectites.[40] There it was concluded that the stacking in montmorillonite was always turbostratic. More work will be necessary to estimate the size of the relative populations of turbostratic vs correlated layer stacking using HREM.
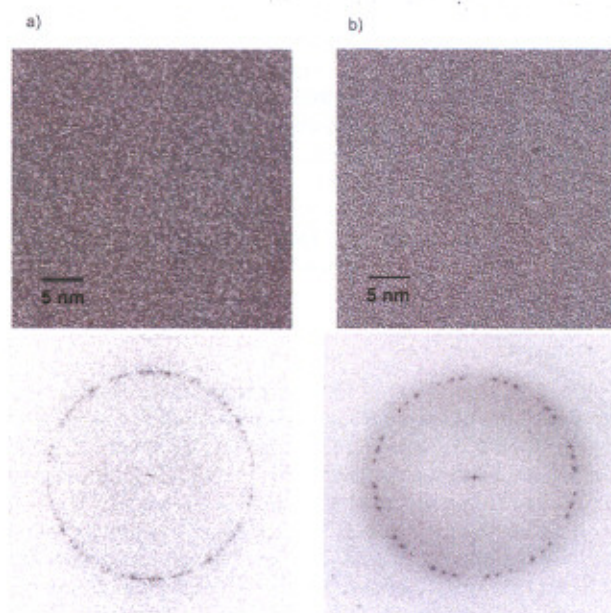
Finally, HREM was also used to study MMT sheet bending. It is important to note that these individual sheets are not rigid plates, but because of high aspect ratios they can be highly flexible and show localized bending. The elastic properties, including the bending stiffness, of single MMT sheets have been
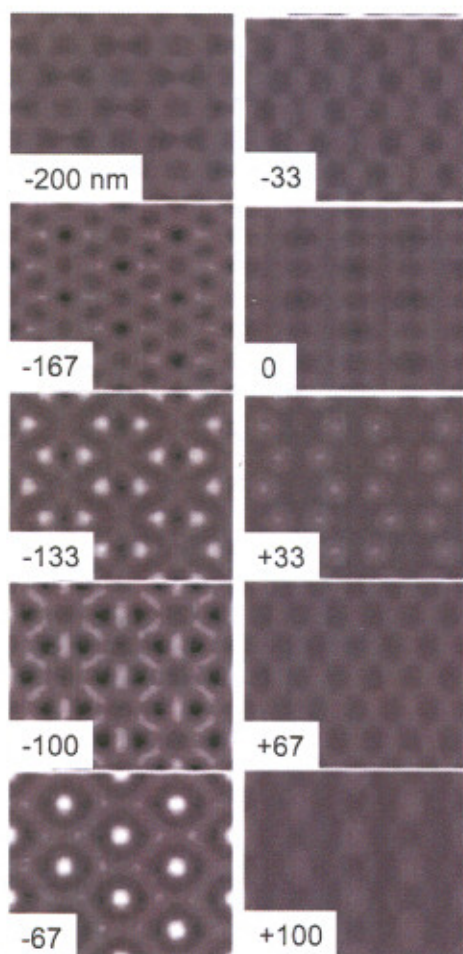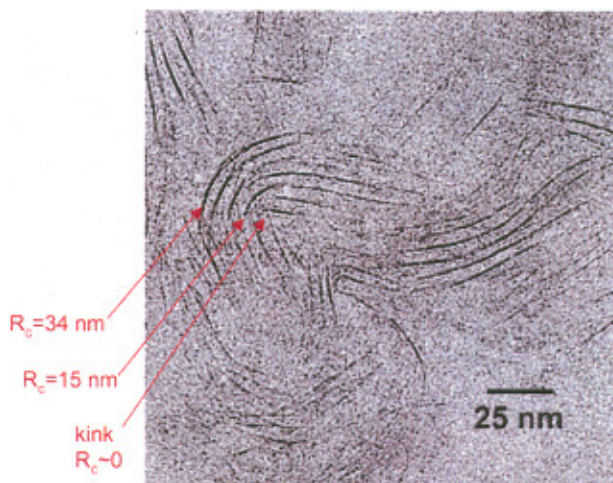
Figure 11. Simulated HREM images from the direction normal to the MMT sheets for a single layer at varying values of defocus. A good match to the experimental data in Figure 10a is seen at a defocus of −100 nm.

Figure 12. Regions of multiple layers showing evidence for both correlated and uncorrelated stacking. The HREM of 20A OMMT (shown in (a)) and its FFT show no clear correlations. The HREM image of the same sample, different region (shown in (b)), shows evidence for interlayer correlations.

Figure 13. Bright-field TEM image of a region of OMMT (I30E) sheets in a nanocomposite showing localized bending.

examined using molecular simulation techniques.[13] Figure 13 shows a region of an intercalated or swollen epoxy/OMMT nanocomposite where the layers are coherently bent. At the outside of the bent stack of intercalated sheets, where the radius of curvature is the largest, uniform bending is seen. Nearer the center of the bent stack the radius of curvature quickly drops and the OMMT sheets form localized kinks. In the following discussion buckling is defined as the failure of a sheet by bending during compressive deformation along the plane of the sheet (Euler buckling). Kinking is defined as the failure of a sheet by severe localization of strain to a single point along the sheet during uniform elastic bending. Srolovitz et al.[63] have investigated the energy balance between coherent bending and localized kinks in crystals, and Kübel et al.[64] have compared the energies of coherent bending vs bending mediated by interlayer slip. In the case of the bent stack of sheets in Figure 13, the radius of curvature, R_c, of the layer at the outside of the stack is approximately 34 nm. For an aluminosilicate layer of thickness $t = 1.0$ nm, this corresponds to a maximum strain of $\epsilon = 0.5(t/R_c) = 0.015$ concentrated at the inside (compressive) and outside (tensile) edges of the bent single sheet.[65] Toward the center of the stack the bending becomes more localized and R_c decreases to 15 nm ($\epsilon = 0.033$). Inside this region, near the inside layers of the stack, a localized kink is formed and R_c is too small to be measured. If we consider one of the inside layers of this stack ($R_c = 15$ nm, $\epsilon = 0.033$) to be the largest strain

tolerable by a single sheet before kinking, this strain would be analogous to a yield or fracture strain for a single sheet in a bending geometry.

Manovitch and Rutlege[13] have simulated the failure of a single MMT sheet during compressive deformation by buckling. The simulation measured the slope of the force vs strain curve (measuring strain as the change in length of the simulation cell divided by the original length), and found this slope to be constant below the buckling strain, where the deformation was elastic and in a uniaxial compressive geometry. Above the buckling strain the sheet bends out of the plane of compression and the slope of the force vs strain curve decreases. This buckling strain was found to be 0.034. This critical failure strain for a single sheet is in good agreement with the critical strain measured here from radius of curvature measurements, although the deformation geometry is different in the two cases.

The simple calculations presented here show that the maximum strain in MMT layers that occurs from bending to high curvatures ($R_c \sim 15$ nm) is still relatively low ($\sim$3%). This low strain arises from the low thickness of the sheet ($\sim$1 nm). Even though the modulus of the sheets is high, it is clearly possible for them to show large amounts of bending. While 100–200 nm in lateral extent (see Figure 9), MMT has been shown to have persistence lengths on the order of only 10 nm in aqueous suspension.[66] Inhomogeneous local stresses due to differences in epoxy curing rates may cause the types of coherent bending shown in Figure 13.

Conclusions

Using a combination of HREM imaging theory and experiment, we have described the procedures necessary to image both the inter- and intrasheet lattice spacings in polymer/layered silicate nanocomposites. This technique allows us to improve the understanding of nanocomposite structure at the 100 nm to subnanometer-length scale. The application of transmission electron microscopy in general to polymer nanocomposites has suffered primarily because of the experimental challenges inherent in the technique. These challenges include reproducibly generating high contrast between the different components in the nanocomposite, as well as relating features in the two-dimensional image to the three-dimensional sample structure. With the use of HREM techniques, we have addressed both of these issues, by controlling the defocus of the microscope to maximize contrast from features of a certain size, as well as direct imaging of the MMT sheets in several orientations (not just "edge on"). Several structural characteristics of the layered silicate filler material were characterized, including experimental verification of the montmorillonite unit cell parameters using HREM, direct visualization of the irregular overall sheet morphology, the low defect density in the sheets themselves, and evidence for some intersheet correlations in stacks of organically modified montmorillonite cast from solution. Significant sheet bending was seen in swollen (intercalated) nanocomposites, and the bending was often coherent, with neighboring sheets having similar contours. Analysis of the radius of curvature in a stack of coherently bent intercalated MMT sheets gave a failure strain in a bending geometry of 0.033.

References and Notes

(1) Ray, S. S.; Okamoto, M. *Prog. Polym. Sci.* **2003**, *28*, 1539−1641.
(2) Alexandre, M.; Dubois, P. *Mater. Sci. Eng.* **2000**, *28*, 1.
(3) Ahmadi, S. J.; Huang, Y. D.; Li, W. *J. Mater. Sci.* **2004**, *39*, 1919−1925.
(4) Pinnavaia, T. J.; Beal, G. W. *Polymer Clay Nanocomposites*; Wiley: New York, 2000.
(5) Usuki, A.; et al. *J. Mater. Res.* **1993**, *8*, 1179−1184.
(6) Kojima, Y.; et al. *J. Mater. Res.* **1993**, *8*, 1185−1189.
(7) Messersmith, P. B.; Giannelis, E. P. *Chem. Mater.* **1994**, *6*, 1719−1725.
(8) Wang, M. S.; Pinnavaia, T. J. *Chem. Mater.* **1994**, *6*, 468−474.
(9) Brown, J. M.; Curliss, D.; Vaia, R. A. *Chem. Mater.* **2000**, *12*, 3376−3384.
(10) Miyagawa, H.; Rich, M. J.; Drzal, L. T. *J. Polym. Sci. B: Polym. Phys.* **2004**, *42*, 4384−4390.
(11) Koerner, H.; Jacobs, D.; Tomlin, D.; Busbee, J.; Vaia, R. *Adv. Mater.* **2004**, *16*, 297−302.
(12) Koerner, H.; et al. *Chem. Mater.* **2005**, *17*, 1990−1996.
(13) Manevitch, O. L.; Rutledge, G. C. *J. Phys. Chem. B* **2004**, *108*, 1428−1435.
(14) Busek, P. R.; Veblen, D. R. Mineralogy. In *High Resolution Transmission Electron Microscopy*; Busek, P. R., Cowley, J. M., Eyring, L., Eds.; Oxford University Press: Oxford, 1992; Chapter 9.
(15) Wang, Z. L. *J. Phys. Chem. B* **2000**, *104*, 1153−1175.
(16) Zhu, S.; Sun, K.; Zhang, Q. Y.; Zu, X. T.; Wang, L. M.; Ewing, R. C. *J. Appl. Phys.* **2003**, *94*, 5648−5651.
(17) Kobayashi, T. *Crystals: Growth, Properties and Application. Organic Crystals I: Characterization*; Karl, N., Freyhardt, H. C., Mueller, G., Eds.; Springer: Berlin, 1991; Vol. 13, pp 1−64.
(18) Martin, D. C.; Thomas, E. L. *Polymer* **1995**, *36*, 1743−1759.
(19) Martin, D. C.; Chen, J.; Yang, J.; Drummy, L. F.; Kübel, C. *J. Polym. Phys. B: Polym. Phys.* **2005**, *43*, 1749−1778.
(20) Voigt-Martin, I. G. *Acta Polym.* **1996**, *47*, 311−322.
(21) Cuisinier, F. J. G.; Steuer, P.; Brisson, A.; Voegel, J. C. *J. Cryst. Growth* **1995**, *156*, 443−453.
(22) Chen, Q. Z.; et al. *Biomaterials* **2004**, *25*, 4243−4254.
(23) Van Tendeloo, G.; Bernaerts, D.; Amelinckx, S. *Carbon* **1998**, *36*, 487−493.
(24) Hashimoto, A.; Suenaga, K.; Gloter, A.; Urita, K.; Iijima, S. *Nature* **2004**, *430*, 870−873.
(25) Tanaka, N.; Yamasaki, J.; Kawai, T.; Pan, H. *Nanotechnology* **2004**, *15*, 1779−1784.
(26) Shiang, J. J.; Kadavanich, A. V.; Grubbs, R. K.; Alivisatos, A. P. *J. Phys. Chem.* **1995**, *99*, 17417−17422.
(27) Yaron-Marcovich, D.; Chen, Y.; Nir, S.; Prost, R. *Environ. Sci. Technol.* **2005**, *39*, 1231−1238.
(28) Clinard, C.; Mandila, T.; Tchoubar, D.; Bergaya, F. *Clays Clay Miner.* **2003**, *51*, 421−429.
(29) Yoonessi, M.; Toghiani, H.; Daulton, T. L.; Lin, J. S.; Pittman, C. U. *Macromolecules* **2005**, *38*, 818−831.
(30) Pradère, P.; Thomas, E. L. *Ultramicroscopy* **1990**, *32*, 149.
(31) Spence, J. C. H. *High Resolution Electron Microscopy*, 3rd ed.; Oxford University Press: Oxford, 2003.
(32) Williams, D. B.; Carter, C. B. *Transmission Electron Microscopy*; Plenum Press: New York, 1996.
(33) Cowley, J. M. Imaging. In *High Resolution Transmission Electron Microscopy and Associated Techniques*; Busek, P. R., Cowley, J. M., Eyring, L., Eds.; Oxford University Press: New York, 1988; Chapter 1.
(34) Handlin, D. L.; Thomas, E. L. *Macromolecules* **1983**, *16*, 1514−1525.
(35) Lednicky, F.; Coufalova, E.; Hromadkova, J.; Delong, A.; Kolarik, V. *Polymer* **2000**, *41*, 4909−4914.
(36) Drummy, L. F.; Yang, J.; Martin, D. C. *Ultramicroscopy* **2004**, *99*, 247−256.
(37) DuChesne, A. *Macromol. Chem. Phys.* **1999**, *200*, 1813−1830.
(38) Heinz, H.; Koerner, H.; Anderson, K. L.; Vaia, R. A.; Farmer, B. L. Submitted for publication in *Chem. Mater.*
(39) Brown, G. *The X-ray Identification and Crystal Structures of Clay Minerals*; Mineralogical Society: London, 1961.
(40) Mering, J. Smectites. In *Soil Components, Vol. 2, Inorganic Components*; Geiseking, J. E., Ed.; Springer-Verlag: New York, 1975.
(41) Moore, D. M.; Reynolds, R. C. *X-ray Diffraction and Identification and Analysis of Clay Minerals*, 2nd ed.; Oxford University Press: Oxford, 1997.
(42) Drits, V. A.; Tchoubar, C. *X-ray Diffraction by Disordered Lamellar Structures*; Springer-Verlag: Berlin, 1990.
(43) Grim, R. E. *Clay Mineralogy*, 2nd ed.; McGraw-Hill: New York, 1968.
(44) Amos, L. A.; Henderson, R.; Unwin, P. N. T. *Prog. Biophys. Mol. Biol.* **1982**, *39*, 183−231.
(45) Kumar, S.; Adams, W. W. *Polymer* **1990**, *31*, 15−19.
(46) Gu, B. X.; Wang, L. M.; Minc, L. D.; Ewing, R. C. *J. Nucl. Mater.* **2001**, *297*, 345−354.
(47) Thilo, E.; Schunemann, H. *Z. Anorg. Allg. Chem.* **1937**, *230*, 321−325.
(48) Grim, R. E.; Bradley, W. F. *J. Am. Ceram. Soc.* **1940**, *23*, 242−248.
(49) Talmon, Y.; Thomas, E. L. *J. Microsc.* **1978**, *113*, 69−75.
(50) Grubb, D. T. *J. Mater. Sci.* **1974**, *9*, 1715.
(51) Wang, S. X.; Wang, L. M.; Ewing, R. C. *Nucl. Instrum. Methods. B* **1998**, *141*, 509−513.
(52) Carter, G. *J. Appl. Phys.* **1996**, *79*, 8285.

17878 *J. Phys. Chem. B, Vol. 109, No. 38, 2005*

Drummy et al.

(53) Rickards, J.; Oliver, A.; José-Yacamán, M. *Ultramicroscopy* **1989**, *30*, 425−428.

(54) Naguib, H. M.; Kelly, R. *Radiat. Eff.* **1975**, *25*, 1.

(55) Wang, L. M.; Ewing, R. C. *MRS Bull.* **1992**, *17*, 38.

(56) Pauling, L. *The Chemical Bond*—A Brief Introduction to Modern Structural Chemistry; Cornell University Press: Ithaca, NY, 1967; p 69.

(57) Cowley, J. M. *Diffraction Physics*; North-Holland: Amsterdam, 1981.

(58) Cowley, J. M.; Moodie, A. F. *Acta Crystallogr.* **1957**, *10*, 609.

(59) Cowley, J. M.; Moodie, A. F. *Acta Crystallogr.* **1959**, *12*, 353.

(60) Cowley, J. M.; Moodie, A. F. *Acta Crystallogr.* **1957**, *12*, 360.

(61) Goodman, P.; Moodie, A. F. *Acta Crystallogr., A* **1974**, *30*, 280.

(62) Hirsch, P.; Howie, A.; Nicholson, R. B.; Pashley, D. W.; Whelan, M. J. *Electron Microscopy of Thin Crystals*; Krieger Publishing: Malabar, FL, 1977; Chapter 7.

(63) Srolovitz, D. J.; Safran, S. A.; Tenne, R. *Phys. Rev. E* **1994**, *49*, 5260.

(64) Kübel, C.; González-Ronda, L.; Drummy, L. F.; Martin, D. C. *J. Phys. Org. Chem.* **2000**, *13*, 816−829.

(65) Stevens, K. K. *Statics & Strength of Materials*, 2nd ed.; Prentice Hall: New York, 1987; p 360.

(66) Schaefer, D. W.; et al. Large-Scale Morphology of Dispersed Layered Silicates. In *Neutron and X-ray Scattering as Probes of Multiscale Phenomena*; Pochan, D., et al., Eds.; Materials Research Society: Warrendale, PA, 2005.